THE JOURNAL OF PHYSICAL CHEMISTRY C
A JOURNAL OF THE AMERICAN CHEMICAL SOCIETY

pubs.acs.org/JPCC
Article

Vibrational Dynamics and Cation Mobility in the TTB Oxide $K_3Li_2Nb_5O_{15}$: A Combined Raman, AIMD, and QTAIM Study

Maria Luisa R. A. Ramalho, Celina Cristian Moura Fonseca, Jeronimo F. Silva, Luíz Eduardo Gomes da Cruz, Gerd Bruno Rocha, André Luiz Menezes de Oliveira, Brendan James Kennedy, Anderson Reis Albuquerque, Julio Ricardo Sambrano, and Ary S. Maia*

Cite This: J. Phys. Chem. C 2025, 129, 13791−13802

Read Online

ACCESS | Metrics & More | Article Recommendations | Supporting Information

ABSTRACT: The $K_3Li_2Nb_5O_{15}$ (KLN) compound, which crystallizes in a tetragonal tungsten bronze (TTB) structure, was synthesized and structurally resolved by the Rietveld refinement of X-ray diffraction (XRD) data, followed by characterization via Raman spectroscopy and theoretical investigation through an integrated computational approach. Density functional theory (DFT) calculations, incorporating the quasi-harmonic approximation and topological analysis based on the quantum theory of atoms in molecules (QTAIM), were employed to interpret vibrational features and to establish the crystal and electronic structures. Theoretical and experimental Raman spectra were compared, revealing significant discrepancies below 400 cm^{-1}. These differences were attributed to the dynamic behavior of K^+ and Li^+ cations within the pentagonal and trigonal channels, respectively. Ab initio molecular dynamics simulations confirmed the high mobility of Li^+ and the site-dependent behavior of K^+, which directly impact the vibrational signatures. The combined vibrational and dynamic analyses suggest that the observed oxygen mobility, particularly in the channel regions, may influence the formation and migration of oxygen vacancies, with possible implications for ionic conductivity, gas sensing, and (photo)catalytic activity in functional oxides. This study provides a detailed atomistic understanding of the coupling between structural dynamics and vibrational spectra in complex TTB frameworks, contributing to deeper insight into phenomena rarely explored at this level.

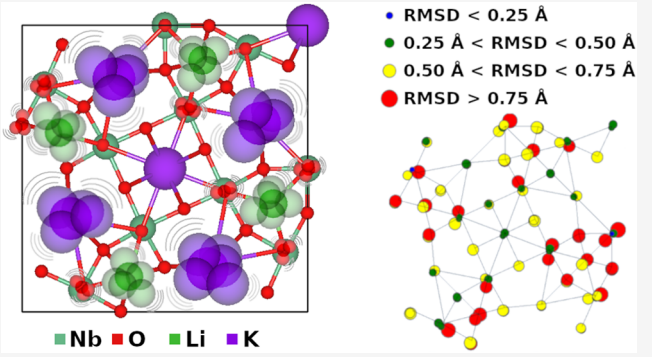

1. INTRODUCTION

Tetragonal tungsten bronze (TTB) structures can be generically represented by the chemical formula $(A1)_2(A2)_4(C)_4(B1)_2(B2)_8O_{30}$. These structures consist of a three-dimensional (3D) framework of corner-sharing $[BO_6]$ octahedra that define channels with three distinct cross-sectional geometries: square (A1 sites), pentagonal (A2 sites), and triangular (C sites).[1−5]

TTB compounds can be classified into three general categories based on their cation occupancy: "stuffed" structures, in which all cation sites are fully occupied; "filled" structures, where the A1 and A2 sites are occupied, while the C sites remain vacant; and "unfilled" structures, characterized by partial occupancy or vacancies in the A1 and/or A2 sites.[6] The complexity of these systems arises from the multitude of possible site occupancies and cation combinations, giving rise to a vast array of TTB derivatives with rich structural and physical behavior.[2−5,7−9]

This structural versatility makes TTB compounds a subject of sustained scientific interest, owing to their wide range of functional properties, such as dielectric response,[10] ferroelectricity,[11,12] piezoelectricity,[12] pyroelectricity,[13] and ionic conductivity.[10] Notably, TTBs constitute the second largest class of ferroelectric materials, surpassed only by perovskites, highlighting their significance in the development of functional oxides.[9] The presence of structurally distinct channels enables compositional tuning and site-specific substitution, allowing for the design of materials with customized dielectric and transport characteristics. Consequently, TTB-type structures have been explored for various applications, including nonlinear optics,[14] energy storage,[5,15] and sensor[16] technologies. Furthermore, their anisotropic frameworks and the possibility of cation mobility render them ideal platforms for probing structure−property relationships through both experimental and computational approaches. In particular, understanding how different cations interact with the channel environment[9] is key to unraveling the mechanisms governing

Received: May 14, 2025
Revised: July 11, 2025
Accepted: July 14, 2025
Published: July 18, 2025

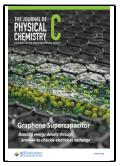

https://doi.org/10.1021/acs.jpcc.5c03313
J. Phys. Chem. C 2025, 129, 13791−13802

ion transport and dynamic structural responses in TTB-based materials.

Potassium lithium niobate ($K_3Li_2Nb_5O_{15}$), or KLN, adopts a stuffed TTB structure under ambient conditions. In its nonpolar aristotype form, the A1 and A2 sites are primarily occupied by potassium ions, while lithium ions fully occupy the C sites. The unit cell, composed of two formula units totaling 50 atoms, includes 10 [NbO_6] octahedra that share corners, each aligned along the crystal's *c*-axis, forming a tetragonal arrangement,[17] as shown in Figure 1.

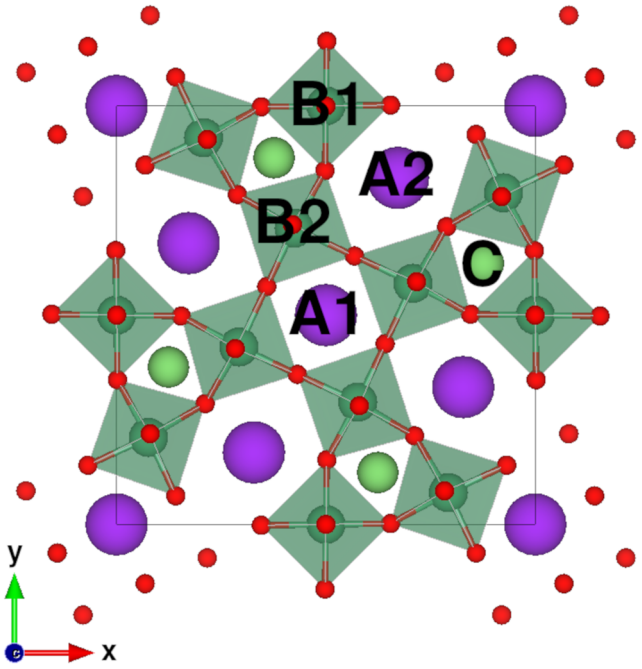

Figure 1. Crystal structure of $K_3Li_2Nb_5O_{15}$ (KLN) in its nonpolar aristotype form, viewed along the *z*-axis. The structure consists of a network of corner-sharing [NbO_6] octahedra with dark green, red, light green, and purple spheres representing Nb, O, Li, and K atoms, respectively.

While several authors designate it as *P4bm*[1,17−20] at room temperature—a polar, noncentrosymmetric space group typically associated with nonstoichiometric potassium lithium niobate—the ICSD database[21] only lists the structure as *P4/mbm*, a nonpolar space group consistent with the stoichiometric composition of KLN.[22] In fact, some studies report a phase transition from *P4bm* to *P4/mbm* around 440 °C.[17,19,20,23]

Given its fully stuffed TTB structure, KLN provides a unique opportunity to investigate cation behavior across all A and C sites without the confounding effects of cation-vacancy interactions or site occupancy competition. This structural completeness reduces the number of variables involved, allowing for a more direct correlation between site-specific dynamics and vibrational responses.[3,9] To the best of our knowledge, no theoretical studies of KLN have been reported in the literature. Therefore, we carried out an integrated theoretical and experimental investigation to better understand this structure.

2. EXPERIMENTAL AND THEORETICAL METHODS

$K_3Li_2Nb_5O_{15}$ (KLN) was synthesized using the modified Pechini method, with potassium nitrate (KNO_3, 99%), lithium carbonate (Li_2CO_3, 99%), and niobium ammonium oxalate ($(NH_4)_2C_2O_4 \cdot H_4O$, 99.5%) as metal precursors. The $K^+/Li^+/Nb^{5+}$ molar ratio was maintained at 3:2:5, with an additional 15% (w/w) excess K^+ to compensate for potassium volatility at high temperatures.

In the first stage, metal citrates were formed by adjusting the solution's pH to approximately 4 with the addition of NH_4OH solution. The second stage involved a polyesterification reaction, where the solution temperature was maintained at 70 °C, while ethylene glycol was slowly added in a 60:40 (w/w) ratio of citric acid to ethylene glycol. The solution was then heated to 100 °C and reduced to one-third of its initial volume, at which point a polymeric resin was obtained. The resulting polymeric resin was pyrolyzed at 300 °C for 2 h and then calcined at 900 °C for 4 h, yielding a white powder.

X-ray diffraction (XRD) measurements were performed at room temperature in a high-resolution STOE STADI P diffractometer equipped with a primary monochromator and Mo Kα1 (λ = 0.71073 Å). The samples were placed in a 0.2 mm glass capillary and rotated during the measurement according to the Debye−Scherrer geometry to minimize preferred orientation effects. The XRD data were collected to $2\Theta = 55°$ using three Mythen detectors.

The structure of the $K_3Li_2Nb_5O_{15}$ (KLN) sample was solved by the Rietveld refinement method as implemented in the GSAS-II software.[24] For the refinements, crystallographic information reported for $K_3Li_2Nb_5O_{15}$ with a tetragonal tungsten bronze-type structure, with space group *P4bm* (#100)-ICSD 125631[25] and *P4/mbm* (#127)-ICSD 164890,[22] was used as the initial model. The refinements were modeled by using a combination of Gaussian and Lorentzian functions, and the background correction was applied by using a Chebyshev-1 polynomial function.

Raman spectroscopy was conducted using an inVia Raman Microscope (Renishaw) confocal Raman spectrometer with a 514 nm argon-ion laser. A spectral resolution of 4 cm^{-1} was employed over the 100−1000 cm^{-1} range.

The KLN structure was optimized using the CRYSTAL17 software[26] at the density functional theory (DFT) level with the B3LYP-D3 functional, starting from the tetragonal *P4/mbm* space group,[22] as specified in the ICSD file 164890. The optimization naturally converged to a structure in the *P4bm* space group, consistent with previous studies.[1,17−20] For comparison, an additional optimization was performed with the same initial structure but was constrained to the *P4/mbm* symmetry. Although partial occupancies are commonly observed in TTB-type structures, KLN was treated as a fully ordered system, consistent with its stuffed TTB nature. This choice avoids the need for large supercells to model configurational disorder and is further justified by the Rietveld refinement, in which no partial occupancies were introduced.

The pob-TZVP rev2 basis sets for all elements were employed, as obtained from the CRYSTAL17 database.[27,28] The accuracy of the Coulomb and exchange series was controlled by five threshold parameters set to 10, 10, 10, 10, and 20. Given the anisotropy of TTB structures,[1,17] a shrink factor of 6 × 6 × 24 was used. The self-consistent field (SCF) convergence criterion was set to an energy threshold of 10^{-10} Hartree.

https://doi.org/10.1021/acs.jpcc.5c03313
J. Phys. Chem. C 2025, 129, 13791−13802

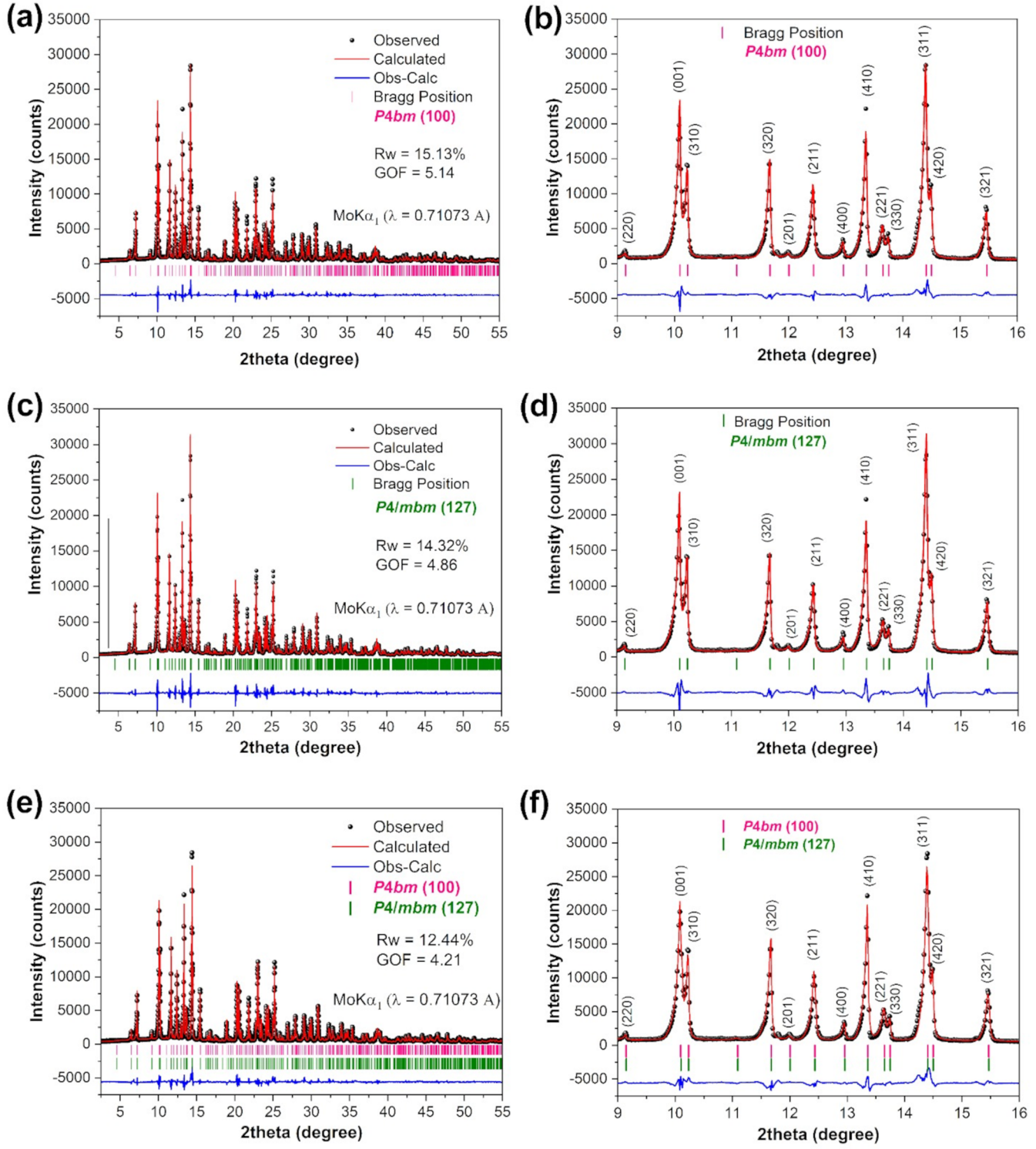

Figure 2. XRD patterns with Rietveld refinement profiles for the KLN sample. The data were modeled to a single phase with (a, b) *P4bm* and (c, d) *P4/mbm* symmetries and to a (e, f) mixture of *P4bm* and *P4/mbm* phases. The selected region of the corresponding patterns (b, d, f) indicates the difference in fit.

Geometry optimizations were carried out using the Broyden–Fletcher–Goldfarb–Shanno (BFGS) algorithm for Hessian updating, with convergence criteria of 0.00001 au for the gradient and 0.00004 au for nuclear displacements.

Vibrational harmonic frequencies were calculated, and the relative Raman intensities of the peaks were determined based on the solution of the first- and second-order coupled-perturbed-Hartree–Fock/Kohn–Sham (CPHF/KS) equations.[29]

The topological analysis, based on quantum theory of atoms in molecules (QTAIM), was developed through the TOPOND module[30] of the CRYSTAL17 package and analyzed by the TopIso3D Viewer software.[31]

https://doi.org/10.1021/acs.jpcc.5c03313
J. Phys. Chem. C 2025, 129, 13791−13802

Table 1. Refined Lattice Parameters (a, b, c) and Unit Cell Volume (V) from the Structural Refinements Using a Single Structural Model for KLN (*P4/mbm* or *P4bm*) As Well As Using a Mixture of *P4/mbm* and *P4bm* Phases

space group	*P4bm*	*P4/mbm*	*P4bm* + *P4/mbm*
phase fraction (%)	100	100	70.8(7)/29.2(7)
$a = b$ (Å)	12.56622(24)	12.56766(23)	12.5674(4)/12.5660(8)
c (Å)	4.02595(10)	4.02616(10)	4.02952(12)/4.01560(19)
vol (Å^3)	635.738(25)	635.917(23)	636.42(4)/634.08(7)
R_{wp} (%)	15.13	14.32	12.44
GOF	5.14	4.86	4.21

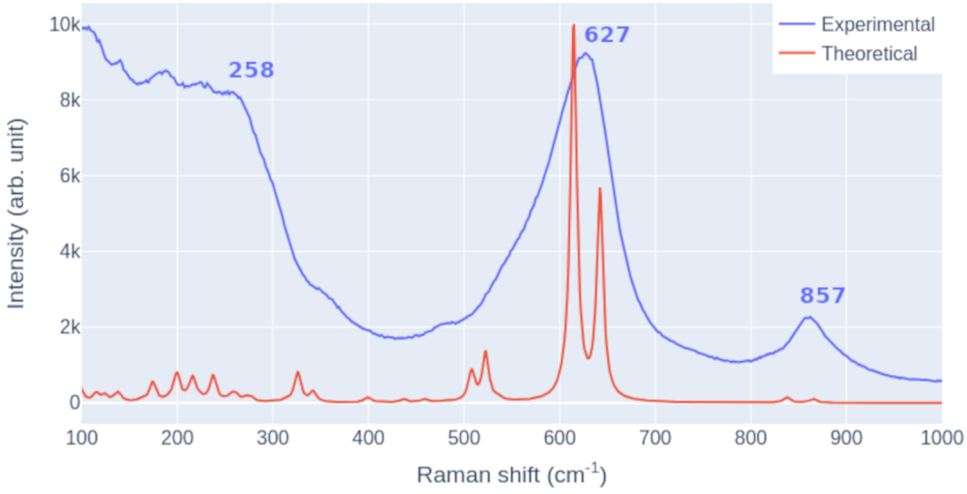

Figure 3. Experimental (blue) and theoretical (red) Raman spectra of KLN between 100 and 1000 cm^{-1}. The computed spectrum was red-shifted by 55 cm^{-1}.

The quasi-harmonic thermal properties of KLN were computed by using the CRYSTAL17 package. By default, the volume variation was set to 3%, and four volumes were considered, meaning vibrational frequencies were calculated at four different volumes, ranging from a −3% compression to a +6% expansion. The four volumes used in this calculation were 617.356, 625.2448, 636.4521, and 675.6912 Å^3. Phonon frequencies were individually fitted as functions of volume using first- and second-order polynomial approximations (default setting).[32]

Ab initio molecular dynamics (AIMD) were performed in the isothermal−isochoric (NVT) ensemble at 300 K using the CP2K code,[33] which employs a localized basis set of Gaussian-type orbital functions for the description of the Kohn−Sham matrix within the framework of the Gaussian plane wave method. The canonical sampling through velocity rescaling (CSVR) thermostat, with a relaxation time of 8 fs, was applied over 5000 steps of 1 fs each, resulting in a total simulation time of 5 ps. A cutoff of 500 Ry is used for the auxiliary basis set of plane waves to expand the electronic density. K, Li, Nb, and O atoms are described by scalar-relativistic norm-conserving Goedecker−Teter−Hutter pseudopotentials[34,35] for including 9, 3, 13, and 6 valence electrons, respectively. Calculations were performed at the γ point using the MOLOPT basis sets[36] optimized for these pseudopotentials, using the PBE exchange−correlation functional. For these AIMD calculations, a 1 × 1 × 2 supercell was constructed from the structure fully optimized by CRYSTAL17, yielding two unit cells with a total of 100 atoms.

Following the molecular dynamics simulation, a clustering analysis was performed on the molecular trajectory to identify the most representative structure and detect the emergence of distinct conformations within the system. For this analysis, the agglomerative hierarchical clustering algorithm was employed using a cutoff distance (epsilon) of 0.5 Å. The clustering was carried out using the CPPTRAJ software.[37]

The MSD and RMSD analyses were performed using the *ab initio* molecular dynamics (AIMD) trajectory of $K_3Li_3Nb_5O_{15}$ at 300 K. MSDs were computed for each atomic species as the average squared displacement from their initial positions over time, enabling the evaluation of atomic mobility and diffusivity trends. Potassium atoms were further categorized by the crystallographic sites they occupy (square and pentagonal channels) to assess the site-specific dynamics. RMSD values were obtained by aligning each frame to the initial structure using a least-squares fit and calculating the root-mean-square displacement across all atoms. All analyses were conducted with the MDAnalysis library (version 2.6.1) and custom Python scripts. In both analyses, the translational motion of the entire system was removed by subtracting the center-of-mass displacement at each step, ensuring that only internal atomic motions were considered.

The radial distribution functions (RDFs) were computed from the AIMD trajectory using the MDAnalysis Python library. The analysis was performed over all trajectory frames, considering a maximum cutoff distance of 6.0 Å and 150 histogram bins. RDFs were calculated between oxygen atoms and each cationic species (Li^+, K^+, and Nb^{5+}), with site-specific differentiation for K^+ cations occupying the A1 (square) and A2 (pentagonal) channels. Atom selections were based on fixed atomic indices derived from the initial structure, and the periodic boundary conditions were applied by using the lattice parameters of the simulated cell.

https://doi.org/10.1021/acs.jpcc.5c03313
J. Phys. Chem. C 2025, 129, 13791−13802

3. RESULTS AND DISCUSSION

Representative Rietveld refinement profiles are presented in Figure 2, illustrating the high quality of the fit between the experimental and calculated X-ray diffraction patterns. The corresponding refined structural parameters are summarized in Table 1.

Table 2. Calculated Frequencies for KLN with Normalized Intensities of >1% and Their Corresponding Normal Vibrational Modes

frequency (cm^{-1})	mode	intensity (%)
133	E	2.06
153	E	3.88
170	E	2.19
179	E	1.75
193	E	2.32
229	E	5.10
255	A_1	7.33
271	A_1	5.35
292	A_1	6.76
312	A_1	1.37
316	A_1	1.51
332	B_1	1.02
381	A_1	8.12
397	A_1	2.58
454	A_1	1.32
563	E	7.97
578	A_1	12.94
670	A_1	100.00
697	A_1	54.86
893	B_2	1.46
920	B_1	1.02

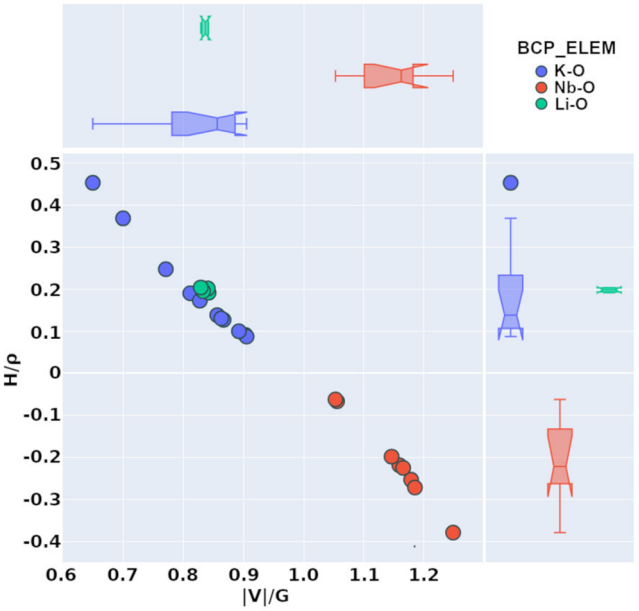

Figure 4. Classification of different KLN bond critical points based on $|V|/G$ vs H/ρ values, calculated by QTAIM theory.

According to the literature, $K_3Li_2Nb_5O_{15}$ adopts a tetragonal tungsten bronze crystal structure, presenting two possible space groups: the *P4bm* phase, which is a ferroelectric phase;[25] and *P4/mbm*, a paraelectric one.[22] The refinements show that both structural models fit well with the experimental XRD pattern (Figure 2a,c). This strong agreement is also evident at the zoom-in on specific diffraction peaks over a 2Θ range of 9−18° (Figure 2b,d). However, an unexpectedly small improvement in the reliability of the overall weighted R-factor (Rw) and goodness-of-fit (GOF) was achieved using the centrosymmetric paraelectric *P4/mbm* phase (Figure 2c). Based on this, refinements were also performed considering mixed phases with *P4bm* and *P4/mbm* space groups (Figure 2e,f). From this refinement, a further improvement in the overall Rw and GOF values was effectively achieved. The unit cell parameters in both phases did not significantly change; however, the amount of the noncentrosymmetric ferroelectric *P4bm* phase remained noticeably higher (Table 1).

Supporting Information (SI) presents the results of computational simulations for both symmetries (*P4bm* and *P4/mbm*), including structural parameters (Figures S1 and S2), atomic positions (Tables S1 and S2), and energy metrics (Table S3) of the optimized structures. The structure optimized in the space group *P4bm* exhibits a total energy of 7 kJ mol^{-1} lower than that of the constrained *P4/mbm* structure, confirming its greater stability. Although a full convex hull analysis is beyond the scope of this work, we note that such an approach could provide complementary insight into the global thermodynamic stability of the system, particularly in the context of competing phases.[38] We highlight this as a valuable direction for future investigations.

Table S4 compares the lattice parameters and unit cell volumes of the *P4bm* and *P4/mbm* structures, as determined experimentally through the Rietveld refinement and theoretically via DFT calculations. The results demonstrate good agreement between the experimentally refined and the DFT-computed values.

The experimental Raman spectrum of the synthesized KLN sample is shown in Figure 3. To interpret this and other spectral features, we rely on theoretical analysis. The KLN compound, with its 50-atom unit cell, exhibits 150 normal vibrational modes, distributed as $21A_1 + 16A_2 + 15B_1 + 20B_2 + 39E(x) + 39E(y)$, with only the A_2 modes being Raman inactive.[39] Comparing the experimental and theoretical spectra provides valuable insights into the vibrational dynamics of the material, particularly the distinct behavior of Li atoms within the trigonal channels of the structure.

The Raman spectra calculated from the DFT-optimized structure, considering different polarizations and different Raman tensor components, are presented in Figure S3. These results reveal a marked anisotropy in the vibrational response of the material. The parallel polarization configuration shows significantly higher intensities compared to the perpendicular one, indicating that the most Raman-active modes are associated with symmetric polarizability changes aligned with the direction of light propagation.

Analysis of the Raman tensor components further supports this anisotropy: the ZZ component exhibits the highest intensity, followed by YY, while XX and off-diagonal terms (XY, XZ, etc.) contribute minimally. This directional dependence suggests that dominant vibrational modes involve polarizability variations primarily along the c crystallographic axis. These findings are consistent with structural features that favor vibrational activity along specific directions and strongly support the anisotropic nature of the Raman response. Importantly, this theoretical behavior reinforces the trends observed in experimental Raman spectra and the literature,[1,17]

https://doi.org/10.1021/acs.jpcc.5c03313
J. Phys. Chem. C 2025, 129, 13791−13802

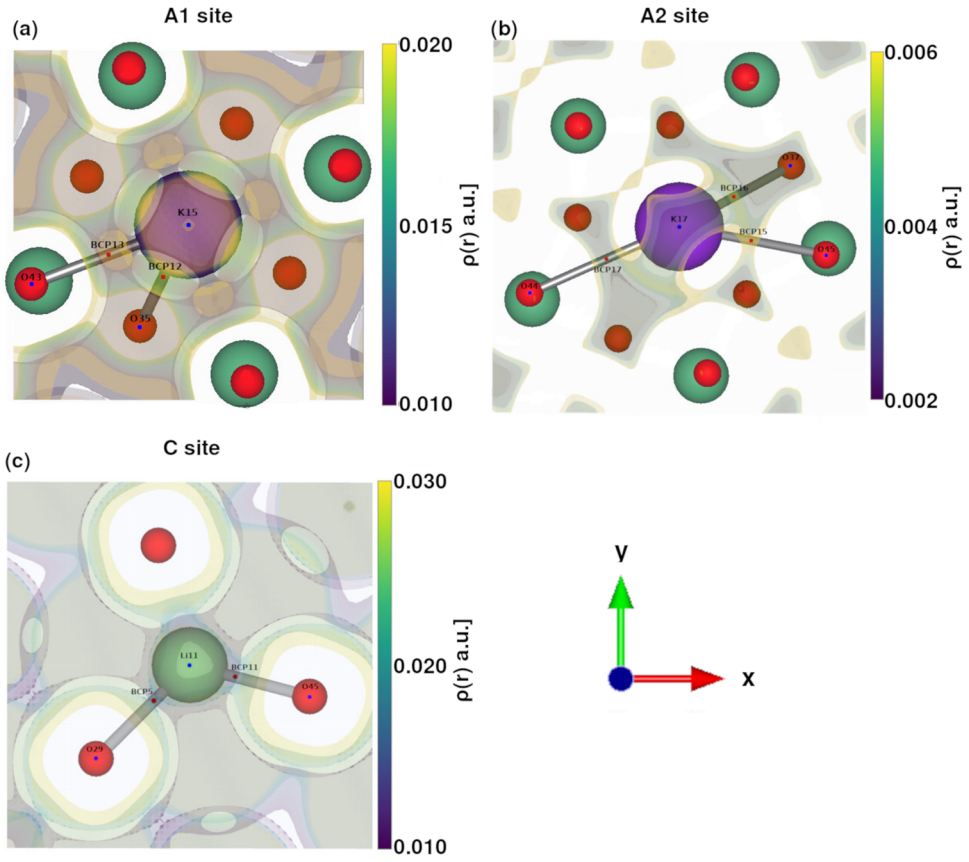

Figure 5. 3D isosurface maps of the electron density around (a) a K^+ cation in the square A1 site, (b) a K^+ cation in the pentagonal A2 site (K17), and (c) a Li^+ cation in the triangular C site (Li11) of the KLN structure, all viewed along the *z*-axis. The isosurface ranges highlight differences in local electronic environments: compact and directional K−O interactions in A1 (0.010−0.020 au), a more diffuse and elongated distribution in A2 (0.002−0.006 au), and short-range, well-defined Li−O interactions in C (0.010−0.030 au). Bond critical points (BCPs) and electron density paths are shown to indicate the nature and strength of these interactions.

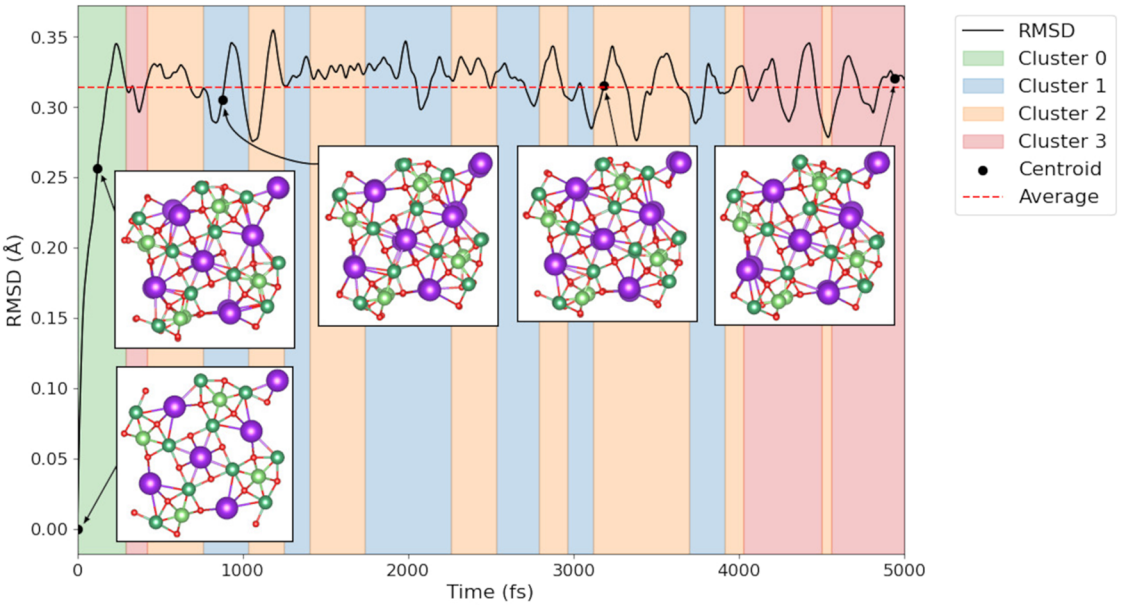

Figure 6. RMSD evolution of $K_3Li_2Nb_5O_{15}$ during AIMD simulation at 300 K. The black curve shows the total RMSD relative to the initial structure. Colored bands indicate cluster assignments based on structural similarity. Representative centroid structures are shown, with black dots marking selected frames, where the first dot denotes the original configuration. The dashed red line indicates the average RMSD over the trajectory.

lending confidence to the computational model and its interpretation of the underlying vibrational dynamics.

Xia et al.[17] employed various scattering geometries to investigate the Raman vibrational spectrum of KLN single

https://doi.org/10.1021/acs.jpcc.5c03313
J. Phys. Chem. C 2025, 129, 13791−13802

Table 3. Clustering Results

cluster	frames	frac	avg dist (Å)	Stdev (Å)	centroid	avg C dist (Å)
0	291	0.058	0.227	0.088	121	0.245
1	1588	0.318	0.199	0.029	876	0.217
2	2079	0.416	0.206	0.027	3184	0.223
3	1043	0.209	0.204	0.040	4945	0.223

crystals. They determined that the [NbO_6] octahedral lattice exhibits six normal vibrational modes: ν_1, ν_2, and ν_3 correspond to stretching modes, while ν_4, ν_5, and ν_6 correspond to bending modes. This set of vibrational modes serves as a signature feature of various niobates with TTB structures.[6,17,22,40] The experimental spectrum (Figure 3) aligns well with those reported in the literature, particularly highlighting the bands at 857 cm^{-1} (ν_1 − Nb−O stretching), 627 cm^{-1} (ν_2 − Nb−O stretching), and 258 cm^{-1} (ν_5 − O−Nb−O bending).

Several authors[6,17,22,40] attributed the peaks observed below 400 cm^{-1} to vibrational modes associated with the relative motion of cations external to the [NbO_6] octahedral framework in various niobates with a TTB structure. Wang et al.[6] further proposed that a significant overlap of multiple modes may arise due to cation movement at A sites in the TTB-filled $Ba_2Ca_{(x)}Na_{(1-2x)}Nb_5O_{15}$ structure, which lacks C site occupancy. Despite the complexity of this spectral region, the experimental data still align well with findings reported by different authors.

As evident in Figure 3, after applying a red shift of 55 cm^{-1} to the computed spectrum to account for systematic deviations between theory and experiment, the agreement between the experimental and computed spectra becomes quite satisfactory in terms of both relative peak positions and intensities. This

Table 4. Summary Statistics of Intercentroid RMSD (in Å) for Each Atomic Species, Including the Initial Configuration at Step 0

element	mean RMSD	max RMSD	min RMSD	pairs > 0.5 Å
Li^+	0.444	0.709	0.185	6
K^+	0.376	0.651	0.109	6
Nb^{5+}	0.282	0.457	0.088	0
O^{2-}	0.465	0.700	0.145	6

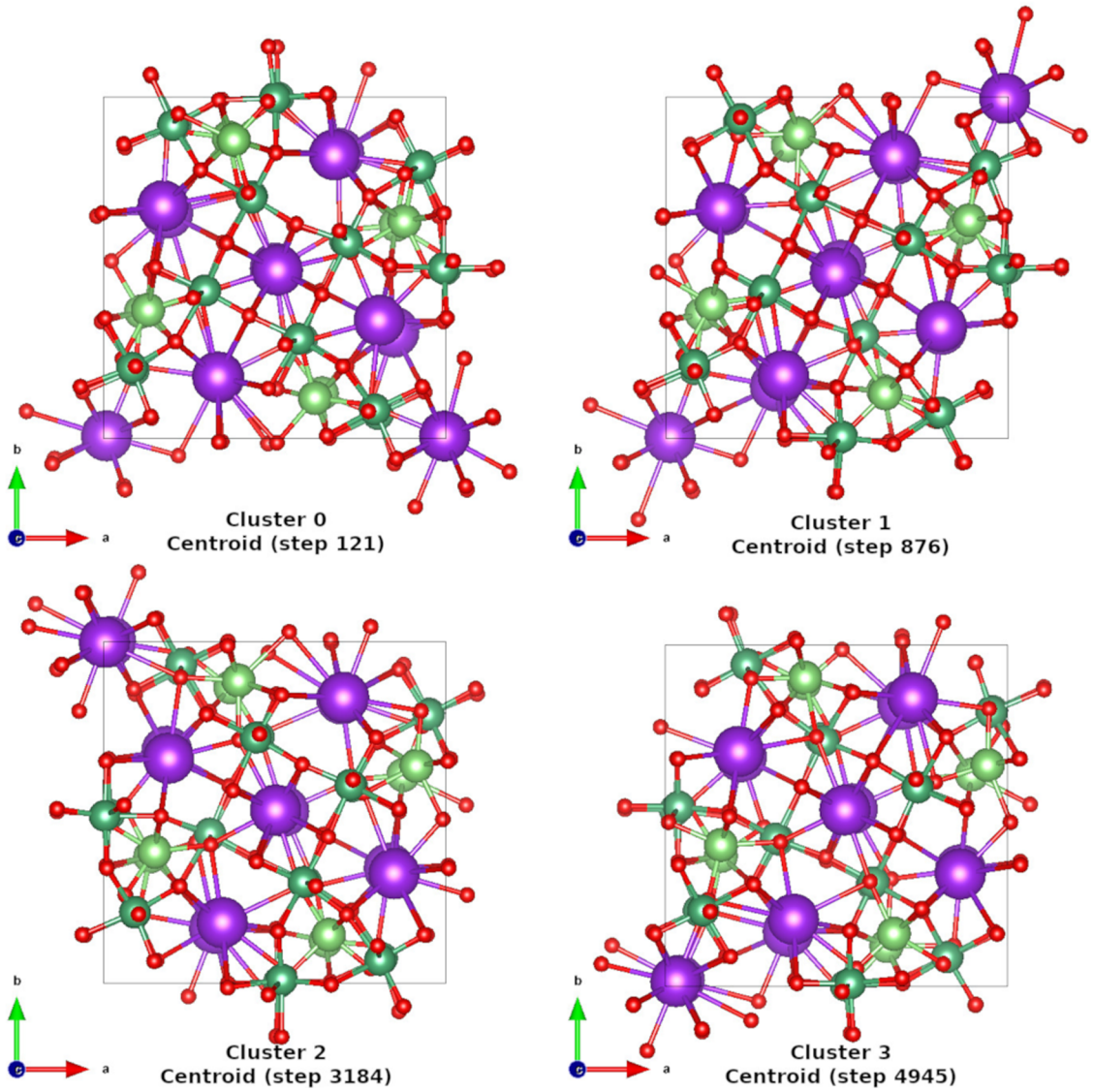

Figure 7. Centroid structures obtained by clustering the AIMD trajectory.

https://doi.org/10.1021/acs.jpcc.5c03313
J. Phys. Chem. C 2025, 129, 13791−13802

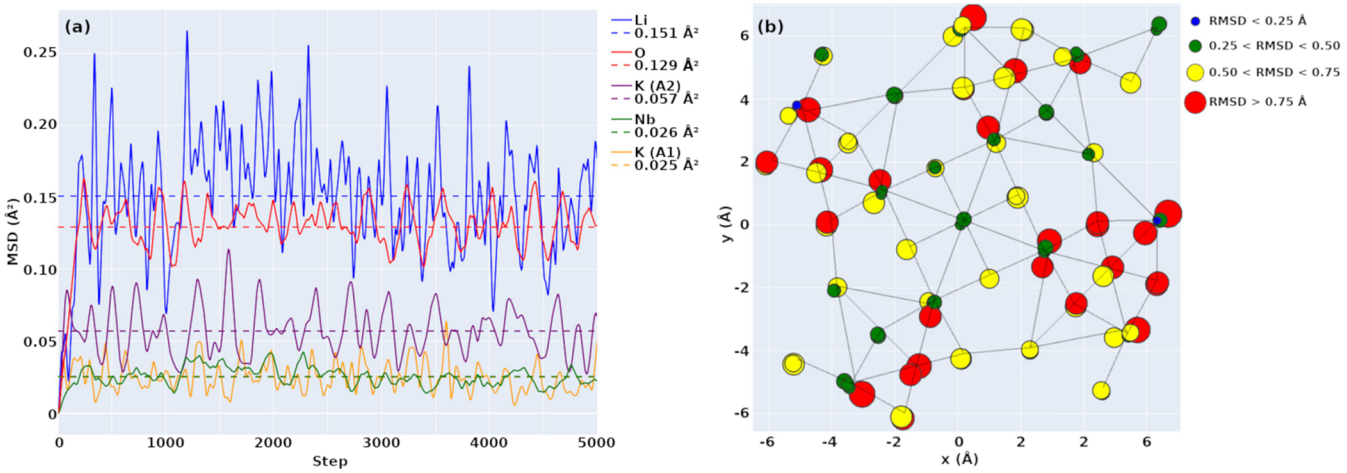

Figure 8. (a) Time evolution of the mean square displacement (MSD) for each atomic species in the $K_3Li_2Nb_5O_{15}$ structure. The two crystallographic sites of K are distinguished: A1 (square channels) and A2 (pentagonal channels). Dashed lines indicate the average MSD values over the simulation for each group. (b) 2D projection of the initial structure highlighting the atomic mobility based on RMSD values. The color code represents different RMSD ranges (blue: RMSD < 0.25 Å; green: 0.25−0.50 Å; yellow: 0.50−0.75 Å; red: > 0.75 Å), and the circle diameter is proportional to the displacement magnitude of each atom.

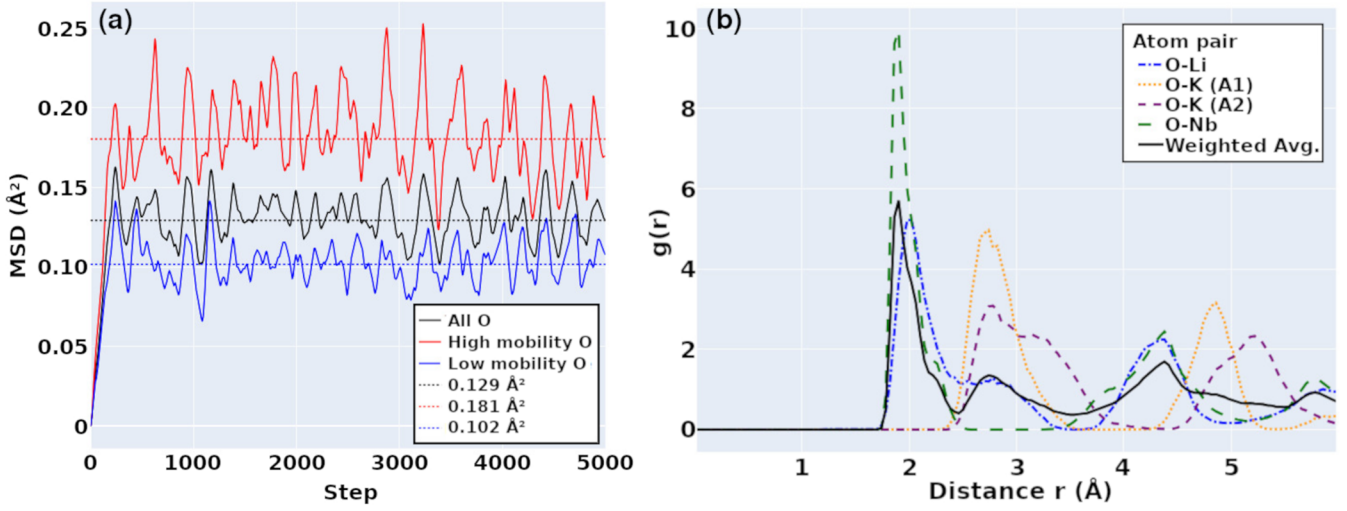

Figure 9. (a) Mean-squared displacement (MSD) curves for oxygen atoms in KLN, shown for all O atoms (black), the most mobile subset (red), and the least mobile subset (blue). Dashed lines indicate average MSD values, highlighting dynamic heterogeneity and the distinction between oxygen atoms near mobile Li^+ and K^+ cations and those in more rigid structural units. (b) Radial distribution functions (RDFs) between oxygen and each cation (Li^+, K^+, and Nb^{5+}), illustrating strong, localized O−Nb interactions and broader O−Li and O−K profiles consistent with higher cation mobility and local disorder.

shift compensates for known limitations in the theoretical approach, such as the harmonic approximation and temperature effects. After applying the red shift, it becomes evident that some of the broader experimental peaks actually correspond to multiple vibrational modes in the theoretical spectrum. However, below 350 cm^{-1}, the experimental spectrum exhibits a notable increase in the intensity of low-wavenumber peaks.

The calculated frequencies with intensities greater than 1% and their corresponding normal vibrational modes are given in Table 2. A complete list of all calculated vibrational modes is provided in Table S5.

The graphical representation of the vectors corresponding to each vibrational frequency listed in Table 2 is shown in Figures S4−S6. Frequencies ranging from 133 to 193 cm^{-1} exhibit a greater contribution from K^+ ions, which occupy the A1 and A2 sites. In contrast, the Li^+ ion, located at the C site, plays a more significant role in the vibrational modes between 229 and 397 cm^{-1}. The remaining frequencies correspond to the vibrational modes of the $[NbO_6]$ octahedral framework, as depicted by the literature.[6,17,22,40]

The significant disparity in the relative intensity of bands below 350 cm^{-1} between the theoretical and experimental spectra may be attributed to the high mobility of cations[6] at sites A1, A2, and C, primarily due to the nature of interactions between K^+ and Li^+ ions and neighboring oxygen atoms.

The optimized KLN structure was analyzed using QTAIM theory to evaluate its bond critical points (BCPs). Table S6 lists the key descriptors calculated for the 23 different BCPs in the system. Based on these results, Figure 4 was created to plot the values of $|V|/G$ vs H/ρ, facilitating the classification of BCPs. These two descriptors are widely recognized in the literature as classic methods for classifying BCPs in crystalline systems.[31,41,42] The dimensionless $|V|/G$ ratio, which compares

https://doi.org/10.1021/acs.jpcc.5c03313
J. Phys. Chem. C 2025, 129, 13791−13802

the electron potential energy density (V) to the kinetic energy density (G), distinguishes three interaction regimes:

(i) A closed-shell (CS) interaction region, where $|V|/G < 1$.

(ii) A shared-shell (SS) interaction region, where $|V|/G > 2$.

(iii) An intermediate transit region between the two.

On the other hand, the quantity H/ρ, defined as the bond degree (BD), represents the total energy (H) per electron density (ρ) at the BCP. In the SS and transit regions, the BD is negative, and its magnitude correlates with bond strength and covalent character. In contrast, the BD is positive in the CS regions, with larger values indicating weaker, closed-shell interactions. Due to these properties, the BD is often referred to as the softening degree (SD) in the CS regions and the covalence degree (CD) in the SS and transit regions.

The results in Figure 4 confirm the greater covalent character of the Nb−O interactions, which form the framework, while the K−O and Li−O interactions exhibit a weaker closed-shell character. It is also interesting to note that compared to the Nb−O and K−O interactions, the Li−O interactions exhibit lower dispersion for both descriptors, while the median values of these descriptors ($|V|/G = 0.837$, $H/\rho = 0.198$) suggest a slightly weaker interaction than the K−O ($|V|/G = 0.886$, $H/\rho = 0.138$).

The greater dispersion observed for the BCPs of the K−O and Nb−O bonds may be attributed to the variety of crystallographic sites occupied by these cations: Nb in B1 and B2 and K in A1 and A2. In particular, for the K−O BCPs, it is noteworthy that the geometrical differences between the sites contribute significantly: the A1 sites, which are quadrangular and thus more spatially constrained, exhibit BCPs that lie closer to the transient region between interaction types, whereas the A2 sites, which are less restrictive, show BCPs characteristic of a closed-shell interaction region.

Figure 5 presents three-dimensional maps of the electron density around the C, A1, and A2 sites, highlighting the low electron density values around the respective BCPs, confirming the weak interactions between the metals (Li and K) and the oxygen atoms.

The QHA (quanti-harmonic approximation) implemented in the CRYSTAL package adjusts individual phonon frequencies, $\omega_{kp}(V)$, as a function of volume using polynomial fits evaluated by the coefficient of determination. Applied to KLN under standard conditions (four volumes), the quadratic fit yielded a strong correlation of 0.9929, while the linear fit had an average correlation coefficient of 0.8708. Frequencies with individual correlation coefficients below 0.8000 for the linear fit and 0.9800 for the quadratic fit were highlighted. The atomic species primarily involved in these poorly correlated vibrational modes are listed in the last column of Table S7. Notably, most of these frequencies correspond to vibrational modes associated with the K and Li atoms at the A1, A2, and C sites.

This result suggests a greater challenge in optimizing the vibrational composition of these atoms across different cell volumes, potentially due to their high mobility.

All of the results presented so far strongly suggest that the discrepancy between the experimental and theoretical Raman spectra is linked to the high mobility of the Li^+ and K^+ cations at the C and A sites, respectively. This mobility may arise from the available free space within the respective channels or from weak Li−O and K−O interactions, as revealed by the low electron density at bond critical points in the QTAIM analysis. To further validate this hypothesis, *ab initio* molecular dynamics (AIMD) calculations were performed using structures fully optimized by the Crystal package in CP2K software.[33]

The simulation, consisting of 5000 steps with a time step of 1 fs each, was conducted in the canonical (NVT) ensemble at 300 K, with a fixed number of particles and volume. The AIMD trajectory was clustered to identify representative centroids of the simulation. The optimal number of clusters was determined to be four based on the elbow method, which showed a clear inflection point at $k = 4$.

Figure 6 illustrates the root-mean-square deviation (RMSD) evolution of $K_3Li_2Nb_5O_{15}$ during the AIMD simulation at 300 K. After an initial equilibration period, the structure fluctuates around a relatively stable average RMSD.

The clustering analysis reveals four distinct structural regimes along the AIMD trajectory, indicating that the system samples different local minima in the configuration space while maintaining the overall structural integrity. These clusters, with respective populations of 5.8, 31.8, 41.6, and 20.9% (Table 3), reflect meaningful conformational variability throughout the simulation. The centroid structures representative of each regime are depicted in Figure 7.

Cluster 0 corresponds to the initial relaxation phase of the system, while clusters 1 and 2 alternate throughout most of the simulation, reflecting dynamic fluctuations between similar metastable configurations. Cluster 3 emerges predominantly from the final segment of the trajectory. To further investigate the structural evolution between these representative configurations—including the initial structure at step 0—intercentroid RMSD matrices and hierarchical clustering were performed (Figures S7−S10).

The results presented in Table 4 confirm that the Li^+ cations exhibit the largest displacements (mean RMSD = 0.444 Å; max = 0.709 Å), with six pairwise comparisons exceeding 0.5 Å. This supports their role as key contributors to the dynamic disorder observed during the simulation. Potassium ions also display significant variations (mean RMSD = 0.376 Å), particularly in later steps, consistent with the enhanced mobility of K^+ in the A2 sites. In contrast, the Nb^{5+} cations remain relatively immobile, with no values above 0.5 Å and tightly grouped centroids, reflecting the structural rigidity of the $[NbO_6]$ framework. Notably, oxygen atoms show extensive rearrangements (mean RMSD = 0.465 Å), second only to Li^+, suggesting that their mobility is strongly coupled to that of nearby cations, especially within the trigonal and pentagonal channels.

Element-resolved MSDs were computed from the trajectory, with the potassium atoms analyzed separately based on the type of site they occupy within the structure (Figure 8a). Based on the MSD values obtained for each crystallographic site, an atomic mobility map was generated to visually represent these variations across the structure, as shown in Figure 8b.

These results confirm the high mobility of Li^+ cations within the narrow trigonal channels, consistent with their small ionic radius, while also revealing a novel finding: the unexpectedly high mobility of certain oxygen atoms. According to the mobility map, among the 26 atoms with the highest displacement (RMSD > 0.75 Å), 5 are Li^+ ions, and the remaining are oxygen atoms located in the vicinity of the trigonal channels.

The elevated and comparable mean MSD values of lithium and oxygen atoms observed in Figure 8a are consistent with this finding. As shown in Figure 9a, the oxygens with the

https://doi.org/10.1021/acs.jpcc.5c03313
J. Phys. Chem. C 2025, 129, 13791−13802

highest mobility exhibit an average MSD higher than that of the Li^+ ions. Interestingly, the behavior of K^+ cations varies significantly, depending on the crystallographic site they occupy. While those located in the square A1 sites exhibit very low average MSD values—comparable to that of niobium—the K^+ cations in the pentagonal A2 sites display notably higher mobility.

This dynamic behavior is well-supported by radial distribution function (RDF) analysis. The detailed RDF profiles are provided in Figure 9b. The O−Nb pairs show sharp peaks close to 2.0 Å, indicative of strong and well-defined bonding, while the O−Li distribution is broader, reflecting the higher mobility of Li^+ in the trigonal channels. The O−K RDF profile further differentiates the K^+ dynamics by site: A1 site K^+ exhibits a sharp peak at 2.9 Å, suggesting structural stability, whereas the broader profile of the A2 site K^+ reflects positional disorder, consistent with the MSD results. These RDF analyses reinforce the notion that both Li^+ and K^+ cations contribute to the vibrational broadening observed in the low-frequency region of the experimental Raman spectrum.

4. CONCLUSIONS

The comparison between experimental and theoretical Raman spectra of $K_3Li_2Nb_5O_{15}$ reveals notable discrepancies below 400 cm^{-1}, where the experimental spectrum shows broad, intense bands absent in harmonic predictions. To address this, a quasi-harmonic approximation was employed, which introduced low-frequency shifts, particularly in the Li−O and K−O modes. However, linear and quadratic volume-dependent fittings for these modes showed poor agreement, indicating the limitations of this approach in capturing the observed spectral broadening. Complementarily, all vibrational modes with intensity above 1% were identified in the harmonic approximation and reported in the SI file. QTAIM analysis highlighted weak electrostatic interactions between mobile cations (Li^+ and K^+) and the framework, suggesting dynamic character. This was confirmed by AIMD simulations at 300 K, which showed significant cation mobility and correlated motion of neighboring oxygens. Clustering of the trajectory revealed transitions between metastable configurations, supporting a picture of dynamic disorder. This combined approach not only explains the broadened spectral features but also offers valuable insight into the vibrational behavior of TTB-type frameworks, where cation dynamics and lattice flexibility are intimately coupled.

■ ASSOCIATED CONTENT

Supporting Information

The Supporting Information is available free of charge at https://pubs.acs.org/doi/10.1021/acs.jpcc.5c03313.

Structural parameters, atomic positions, and energy metrics from DFT optimizations of both *P4bm* and *P4/mbm* symmetries; theoretical Raman spectra under different polarization conditions and tensor components; full list of calculated vibrational modes; vector representations of Raman-active vibrational modes; QTAIM descriptors for all bond critical points; quasi-harmonic approximation (QHA) results; intercentroid RMSD matrices and hierarchical clustering from AIMD trajectories (PDF)

■ AUTHOR INFORMATION

Corresponding Author

Ary S. Maia − *NPE-LACOM, Federal University of Paraíba, João Pessoa, PB 58051-900, Brazil;* orcid.org/0000-0002-5930-790X; Phone: +55(83)32167441; Email: arymaia@quimica.ufpb.br

Authors

Maria Luisa R. A. Ramalho − *NPE-LACOM, Federal University of Paraíba, João Pessoa, PB 58051-900, Brazil*

Celina Cristian Moura Fonseca − *NPE-LACOM, Federal University of Paraíba, João Pessoa, PB 58051-900, Brazil*

Jeronimo F. Silva − *NPE-LACOM, Federal University of Paraíba, João Pessoa, PB 58051-900, Brazil*

Luíz Eduardo Gomes da Cruz − *LQQC, Chemistry Department, Federal University of Paraíba, João Pessoa, PB 58051-900, Brazil*

Gerd Bruno Rocha − *LQQC, Chemistry Department, Federal University of Paraíba, João Pessoa, PB 58051-900, Brazil;* orcid.org/0000-0001-9805-9497

André Luiz Menezes de Oliveira − *NPE-LACOM, Federal University of Paraíba, João Pessoa, PB 58051-900, Brazil; LSQM, Department of Materials Engineering, Federal University of Rio Grande do Norte, Natal, RN 59078-900, Brazil;* orcid.org/0000-0002-7930-6234

Brendan James Kennedy − *School of Chemistry, The University of Sydney, Sydney, NSW 2006, Australia;* orcid.org/0000-0002-7187-4579

Anderson Reis Albuquerque − *Institute of Chemistry, Federal University of Rio Grande do Norte, Natal, RN 59078-900, Brazil;* orcid.org/0000-0001-7727-266X

Julio Ricardo Sambrano − *Modeling and Molecular Simulation Group, São Paulo State University, Bauru, SP 17033-360, Brazil;* orcid.org/0000-0002-5217-7145

Complete contact information is available at: https://pubs.acs.org/10.1021/acs.jpcc.5c03313

Funding

The Article Processing Charge for the publication of this research was funded by the Coordenacao de Aperfeicoamento de Pessoal de Nivel Superior (CAPES), Brazil (ROR identifier: 00x0ma614).

Notes

The authors declare no competing financial interest.

■ ACKNOWLEDGMENTS

The authors thank the financial support from the Brazilian agencies and networks: Conselho Nacional de Desenvolvimento Científico e Tecnológico (CNPq), Coordenação de Aperfeiçoamento de Pessoal de Nível Superior-Brasil (CAPES), Fundação de Apoio a Pesquisa do Estado da Paraíba (FAPESQ-PB), Programa de Apoio a Núcleos de Excelência (PRONEX-FAPESQ), Fundação de Apoio ao Desenvolvimento da Universidade Federal de Pernambuco (FADE-UFPE), and Financiadora de Estudos e Projetos (FINEP). The authors also acknowledge the physical structure and computational support provided by Universidade Federal da Paraíba (UFPB), the computer resources of the Center for Scientific Computing (NCC/GridUNESP) and the Molecular Simulations Laboratory (LSM) of the São Paulo State University (UNESP), Centro Nacional de Processamento de Alto Desempenho em São Paulo (CENAPAD-SP), Núcleo de

Processamento de Alto Desempenho da Universidade Federal do Rio Grande do Norte (NPAD/UFRN), and Supercomputer Santos Dumont at https://sdumont.lncc.br/. G.B.R. acknowledges support from the Brazilian National Council for Scientific and Technological Development (CNPq grant nos. 309761/2017-4, 307340/2021-0, 405745/2021-4, and 440363/2022-5), Fundação de Apoio a Pesquisa do Estado da Paraíba (FAPESQ-PB) (grant no. 030/2023), and Universidade Federal da Paraíba (UFPB) (grant no. PIA14864-2021). J.R.S. thanks the Brazilian funding agencies FAPESP (22/03959-6) and CNPq(307213/2021-8) A.L.M.O. acknowledges the National Council for Scientific and Technological Development CNPq, Brazil (Grant 102504/2024-5). B.J.K. thanks the support of the Australian Research Council.

REFERENCES

(1) Abrahams, S. C.; Jamieson, P. B.; Bernstein, J. L. Ferroelectric Tungsten Bronze-Type Crystal Structures. III. Potassium Lithium Niobate $K_{(6-x-y)}Li_{(4+x)}Nb_{(10+y)}O_{30}$. *J. Chem. Phys.* **1971**, *54*, 2355−2364.

(2) Yao, Y.; Mak, C. Effects of Ca-dopant on the pyroelectric, piezoelectric and dielectric properties of $(Sr_{0.6}Ba_{0.4})_4Na_2Nb_{10}O_{30}$ ceramics. *J. Alloys Compd.* **2012**, *544*, 87−93.

(3) Olsen, G. H.; Selbach, S. M.; Grande, T. On the energetics of cation ordering in tungsten-bronze-type oxides. *Phys. Chem. Chem. Phys.* **2015**, *17*, 30343−30351.

(4) Yang, B.; Wei, L.; Chao, X.; Wang, Z.; Yang, Z. Role of structural modulation in electrical properties of tungsten bronze $(Ca_{0.28}Ba_{0.72})_{2.50.5x}Na_xNb_5O_{15}$ ceramics. *J. Alloys Compd.* **2015**, *632*, 368−375.

(5) Tidey, J. P.; Dey, U.; Sanchez, A. M.; Chen, W.-T.; Chen, B.-H.; Chuang, Y.-C.; Fernandez-Diaz, M. T.; Bristowe, N. C.; Beanland, R.; Senn, M. S. Structural origins of dielectric anomalies in the filled tetragonal tungsten bronze $Sr_2NaNb_5O_{15}$. *Commun. Mater.* **2024**, *5*, No. 71.

(6) Wang, X.; Yang, B.; Yue, J. Critical role of lattice vacancies in A1-site induced by Ca^{2+}-doping on relaxor behavior and electric properties in tungsten bronze $Ba_2NaNb_5O_{15}$ ferroelectrics. *Ceram. Int.* **2023**, *49*, 30853−30863.

(7) Van Uitert, L.; Levinstein, H.; Rubin, J.; Capio, C.; Dearborn, E.; Bonner, W. Some characteristics of niobates having "filled" tetragonal tungsten bronze-like structures. *Mater. Res. Bull.* **1968**, *3*, 47−57.

(8) Whittle, T. A.; Schmid, S.; Howard, C. J. Octahedral tilting in the tungsten bronzes. Addendum. *Acta Crystallogr., Sect. B:Struct. Sci., Cryst. Eng. Mater.* **2018**, *74*, 742−744.

(9) Zeiger, C. R.; Eggestad, K.; Walker, J.; Einarsrud, M.-A.; Williamson, B. A.; Grande, T. Quantifying Emptiness: On the Size of A-Site Vacancies in Tetragonal Tungsten Bronzes. *Chem. Mater.* **2025**, *37*, 3245−3259.

(10) Kakimoto, K.-I.; Kato, H.; Yoshifuji, T.; Ohsato, H. Sintering and Dielectric Property of (K 1- x Na x) Ba 2 Nb 5 O 15 Ceramics. *Ferroelectrics* **2008**, *368*, 179−184.

(11) Sekhar, B. C.; Lakshmi, B. D.; Raju, M. R.; Ramesh, S.; Rao, P. S.; Rao, B. P. Synthesis, structural and microstructural properties of CBN ferroelectric ceramics. *Ferroelectrics* **2021**, *573*, 154−165.

(12) Cai, K.; Jiang, F.; Deng, P.; Ma, J.; Guo, D. Enhanced ferroelectric phase stability and high temperature piezoelectricity in PN ceramics via multisite co-doping. *J. Am. Ceram. Soc.* **2015**, *98*, 3165−3172.

(13) Yao, Y.; Guo, K.; Bi, D.; Tao, T.; Liang, B.; Mak, C.; Lu, S. Pyroelectric properties of calcium doped strontium barium niobate ceramics Sr 0.65- x Ca x Ba 0.35 Nb 2 O 6 (x = 0.05−0.425). *J. Mater. Sci.: Mater. Electron.* **2018**, *29*, 17777−17785.

(14) Chu, S.; Lin, K.; Yang, T.; Yu, C.; Cao, Y.; Zhang, Y.; Sun, Y.; Li, Z.; Jiang, X.; Lin, Z.; et al. Large nonlinear optical effect in tungsten bronze structures via Li/Na cross-substitutions. *Chem. Commun.* **2020**, *56*, 8384−8387.

(15) Yang, B.; Gao, Y.; Li, J.; Wei, J.; Zhu, X.; Qiao, W.; Lyu, J.; Guo, J.; Hu, Y.; Sun, S.; et al. Tailoring Zr-doped tungsten bronze (Sr, Ba, Gd) Nb2O6 relaxor ferroelectric with high electrical insulation interface for dielectric capacitor. *Composites, Part B* **2024**, *271*, 111189.

(16) Li, M.; Shi, Y.; Zhao, C.; Yang, F.; Li, Q.; Zhang, X.; Wu, S.; Chen, H.; Liu, J.; Wei, T. Up-conversion luminescence, thermometry, and optical heating properties of Er 3+-and Yb 3.-doped K 2 LaNb 5 O 15 submicro-particles synthesized by a simple molten salt method. *Dalton Trans.* **2018**, *47*, 11337−11345.

(17) Xia, H. R.; Yu, H.; Yang, H.; Wang, K. X.; Zhao, B. Y.; Wei, J. Q.; Wang, J. Y.; Liu, Y. G. Raman and infrared reflectivity spectra of potassium lithium niobate single crystals. *Phys. Rev. B* **1997**, *55*, No. 14892.

(18) Fortin, W.; Kugel, G.; Rytz, D. Effects of non-stoichiometry on Raman spectra of $K_6Li_4Nb_{10}O_{30}$ (KLN) compounds. *Ferroelectrics* **1997**, *202*, 131−138.

(19) Belboukhari, A.; Abkhar, Z.; Gagou, Y.; Belhadi, J.; Elmoznine, R.; Mezzane, D.; El Marssi, M.; Luk'yanchuk, I. Dielectric properties and relaxation phenomena in the diffuse ferroelectric phase transition in $K_3Li_2Nb_5O_{15}$ ceramic. *Eur. Phys. J. B* **2012**, *85*, No. 215.

(20) Allouche, B.; Gagou, Y.; Belboukhari, A.; Le Marrec, F.; El Marssi, M. Structural and electrical properties of $K_3Li_2Nb_5O_{15}$ thin film grown by pulsed laser deposition. *Mater. Res. Bull.* **2017**, *94*, 287−290.

(21) Karlsruhe, F. Inorganic Crystal Structure Database (ICSD) record 2025 https://icsd.products.fiz-karlsruhe.de/en/about/about-icsd. (Data Release 2025.1. Accessed January 30, 2025).

(22) Ferriol, M.; Cochez, M.; Aillerie, M. Ternary system Li_2O−K_2O−Nb_2O_5: Re-examination of the 30 mol % K_2O isopleth and growth of fully stoichiometric potassium lithium niobate single crystals by the micro-pulling down technique. *J. Cryst. Growth* **2009**, *311*, 4343−4349.

(23) Simon, A.; Ravez, J. Solid-state chemistry and non-linear properties of tetragonal tungsten bronzes materials. *C. R. Chim.* **2006**, *9*, 1268−1276.

(24) Toby, B. H.; Von Dreele, R. B. GSAS-II: the genesis of a modern open-source all purpose crystallography software package. *J. Appl. Crystallogr.* **2013**, *46*, 544−549.

(25) Yoon, D.; Shur, C.; Fukuda, T. Phase matched wavelength dependent on atomic displacement in potassium lithium niobate crystals grown by micro pulling down method. *Cryst. Res. Technol.* **1998**, *33*, 59−64.

(26) Dovesi, R.; Erba, A.; Orlando, R.; Zicovich-Wilson, C. M.; Civalleri, B.; Maschio, L.; Rérat, M.; Casassa, S.; Baima, J.; Salustro, S.; Kirtman, B. Quantum-mechanical condensed matter simulations with CRYSTAL. *WIREs Comput. Mol. Sci.* **2018**, *8*, No. e1360.

(27) Sophia, G.; Baranek, P.; Sarrazin, C.; Rerat, M.; Dovesi, R. Systematic Influence of Atomic Substitution on the Phase Diagram of ABO3 Ferroelectric Perovskites 2023 https://www.crystal.unito.it/basis_sets.html. (Accessed March 30, 2024).

(28) Laun, J.; Bredow, T. BSSE-corrected consistent Gaussian basis sets of triple-zeta valence with polarization quality of the fifth period for solid-state calculations. *J. Comput. Chem.* **2022**, *43*, 839−846.

(29) Pascale, F.; Zicovich-Wilson, C. M.; Gejo, F. L.; Civalleri, B.; Orlando, R.; Dovesi, R. The calculation of the vibrational frequencies of crystalline compounds and its implementation in the CRYSTAL code. *J. Comput. Chem.* **2004**, *25*, 888−897.

(30) Cossard, A.; Desmarais, J. K.; Casassa, S.; Gatti, C.; Erba, A. Charge Density Analysis of Actinide Compounds from the Quantum Theory of Atoms in Molecules and Crystals. *J. Phys. Chem. Lett.* **2021**, *12*, 1862−1868.

(31) Silva, J. F.; Fabris, G. S. L.; Sambrano, J. R.; Albuquerque, A. R.; Maia, A. S. TopIso3D Viewer: Enhancing Topological Analysis through 3D Isosurfaces. *J. Chem. Inf. Model.* **2023**, *63*, 1999−2013.

https://doi.org/10.1021/acs.jpcc.5c03313
J. Phys. Chem. C 2025, 129, 13791−13802

(32) Erba, A. On combining temperature and pressure effects on structural properties of crystals with standard ab initio techniques. *J. Chem. Phys.* **2014**, *141*, No. 124115.
(33) Kühne, T. D.; Iannuzzi, M.; Del Ben, M.; Rybkin, V. V.; Seewald, P.; Stein, F.; Laino, T.; Khaliullin, R. Z.; Schütt, O.; Schiffmann, F.; et al. CP2K: An electronic structure and molecular dynamics software package - Quickstep: Efficient and accurate electronic structure calculations. *J. Chem. Phys.* **2020**, *152*, No. 194103.
(34) Goedecker, S.; Teter, M.; Hutter, J. Separable dual-space Gaussian pseudopotentials. *Phys. Rev. B* **1996**, *54*, No. 1703.
(35) Hartwigsen, C.; Goedecker, S.; Hutter, J. Relativistic separable dual-space Gaussian pseudopotentials from H to Rn. *Phys. Rev. B* **1998**, *58*, No. 3641.
(36) VandeVondele, J.; Hutter, J. Gaussian basis sets for accurate calculations on molecular systems in gas and condensed phases. *J. Chem. Phys.* **2007**, *127*, No. 114105.
(37) Roe, D. R.; Cheatham, T. E. I. PTRAJ and CPPTRAJ: Software for Processing and Analysis of Molecular Dynamics Trajectory Data. *J. Chem. Theory Comput.* **2013**, *9*, 3084−3095.
(38) Sun, W.; Dacek, S. T.; Ong, S. P.; Hautier, G.; Jain, A.; Richards, W. D.; Gamst, A. C.; Persson, K. A.; Ceder, G. The thermodynamic scale of inorganic crystalline metastability. *Sci. Adv.* **2016**, *2*, No. e1600225.
(39) Siapkas, D.; Clarke, R. The Polarised Raman Spectra of Ferroelectric and Non-Ferro-electric Potassium Lithium Niobate. *Phys. Status Solidi B* **1974**, *62*, 43−50, DOI: 10.1002/pssb.2220620103.
(40) Xu, S.; Deng, Z.; Shen, S.; Wei, L.; Yang, Z. Structural and electrical effects of Ag substitution in tungsten bronze $Sr_2Ag_xNa_{1-x}Nb_5O_{15}$ ceramics. *Ceram. Int.* **2020**, *46*, 13997−14004.
(41) Espinosa, E.; Alkorta, I.; Elguero, J.; Molins, E. From weak to strong interactions: A comprehensive analysis of the topological and energetic properties of the electron density distribution involving X−H-F−Y systems. *J. Chem. Phys.* **2002**, *117*, 5529−5542.
(42) Gatti, C. Chemical bonding in crystals: new directions. *Z. Kristallogr. - Cryst. Mater.* **2005**, *220*, 399−457.

https://doi.org/10.1021/acs.jpcc.5c03313
J. Phys. Chem. C 2025, 129, 13791−13802